

This is an Open Access document downloaded from ORCA, Cardiff University's institutional repository: <https://orca.cardiff.ac.uk/id/eprint/156295/>

This is the author's version of a work that was submitted to / accepted for publication.

Citation for final published version:

Shehu, Mustapha, Oladipo, Tolani T., Baffa, Farouk U., Abdullahi, Tahir, Ugwu, Chibuike K., Tanimu, Amina M., Adegboyega, Jide, Korir, Gideon K., Odoguje, Isyaku A. and Dzade, Nelson Y. 2023. First-principles insights into sulfur oxides (SO₂ and SO₃) adsorption and dissociation on layered iron sulfide (FeS) catalyst. *Materials Today Communications* 34 , 105452. 10.1016/j.mtcomm.2023.105452

Publishers page: <https://doi.org/10.1016/j.mtcomm.2023.105452>

Please note:

Changes made as a result of publishing processes such as copy-editing, formatting and page numbers may not be reflected in this version. For the definitive version of this publication, please refer to the published source. You are advised to consult the publisher's version if you wish to cite this paper.

This version is being made available in accordance with publisher policies. See <http://orca.cf.ac.uk/policies.html> for usage policies. Copyright and moral rights for publications made available in ORCA are retained by the copyright holders.



First-principles insights into sulfur oxides (SO₂ and SO₃) adsorption and dissociation on layered iron sulfide (FeS) catalyst

Mustapha Shehu, Tolani T. Oladipo, Farouk U. Baffa, Tahir Abdullahi, Chibuike K. Ugwu, Amina M. Tanimu, Jide Adegboyega, Gideon K. Korir, Isyaku A. Odoguje, Nelson Y. Dzade



PII: S2352-4928(23)00142-3

DOI: <https://doi.org/10.1016/j.mtcomm.2023.105452>

Reference: MTCOMM105452

To appear in: *Materials Today Communications*

Received date: 27 November 2022

Revised date: 13 January 2023

Accepted date: 17 January 2023

Please cite this article as: Mustapha Shehu, Tolani T. Oladipo, Farouk U. Baffa, Tahir Abdullahi, Chibuike K. Ugwu, Amina M. Tanimu, Jide Adegboyega, Gideon K. Korir, Isyaku A. Odoguje and Nelson Y. Dzade, First-principles insights into sulfur oxides (SO₂ and SO₃) adsorption and dissociation on layered iron sulfide (FeS) catalyst, *Materials Today Communications*, (2022) doi:<https://doi.org/10.1016/j.mtcomm.2023.105452>

This is a PDF file of an article that has undergone enhancements after acceptance, such as the addition of a cover page and metadata, and formatting for readability, but it is not yet the definitive version of record. This version will undergo additional copyediting, typesetting and review before it is published in its final form, but we are providing this version to give early visibility of the article. Please note that, during the production process, errors may be discovered which could affect the content, and all legal disclaimers that apply to the journal pertain.

First-principles insights into sulfur oxides (SO₂ and SO₃) adsorption and dissociation on layered iron sulfide (FeS) catalyst

Mustapha Shehu^a, Tolani T. Oladipo^a, Farouk U. Baffa^a, Tahir Abdullahi^a, Chibuike K. Ugwu^a, Amina M. Tanimu^a, Jide Adegboyega^a, Gideon K. Korir^a, Isyaku A. Odoguje^a, Nelson Y. Dzade^{a,b,c*}

^a*Department of Theoretical and Applied Physics, African University of Science and Technology, Km 10 Airport Road, Galadimawa, Abuja F.C.T. 900107, Nigeria*

^bCardiff University, Main Building, Park Place, CF10 3AT, Cardiff, United Kingdom

^c*Department of Energy and Mineral Engineering, Pennsylvania State University, University Park, State College, PA 16802, United States*

ABSTRACT

The adsorption of sulfur oxides (SO_x) represents the fundamental step towards their conversion to lower-risk sulfur-containing species. Herein, we investigate the adsorption and dissociation mechanism of sulfur dioxide (SO₂) and sulfur trioxide (SO₃) on layered iron sulfide (FeS) nanocatalyst (001), (011), and (111) surfaces using density functional theory methodology. Both SO₂ and SO₃ exhibit strong reactivity towards the (011) and (111) surfaces, the with the most stable geometry for SO₂ and SO₃ on the (011) surface predicted to be a tridentate η_2^3 (S,O,O) and a bidentate η_2^2 (O,O) configuration, respectively, whereas on the (111) surface, they are predicted to be coordinated in a monodentate η_2^1 (S) and η_2^1 (O) geometry, respectively. Significant charge donation from the FeS surface to the SO_x species is observed, which resulted in elongation of S–O bond lengths, confirmed by vibrational frequency analyses. Favourable reaction energy and activation barrier is predicted for SO₂ dissociation at the (111) surface.

KEYWORDS: sulfur oxides (SO_x), adsorption, dissociation, layered iron sulfides, DFT

Corresponding Authors: NYD (nxd5313@psu.edu)

1. INTRODUCTION

The removal of sulfur oxides (SO_x) is important from both environmental and human respiratory health protection aspects.¹⁻⁴ Owing to their acidic properties, SO_2 and SO_3 are responsible for acid rain and photochemical smog formation, acidification of soil and water bodies, and corrosion of buildings.^{5,6} Short-term and long-term exposures to SO_x has been linked to an array of adverse respiratory effects including breathing difficulties, aggravated asthma conditions and worsened existing cardiovascular diseases.^{7,8} For this reason, a very strict curb on SO_2 emission limit of 75 ppb in a 1-hr period is enforced by the United States Environmental Protection Agency (US EPA 2018).⁹

To decrease emissions of sulfur oxides into the atmosphere, there is urgent need to develop novel techniques that can effectively remove harmful sulfur oxides (DeSO_x). Various mitigation approaches including the commonly used wet flue gas desulfurization (WFGD)¹⁰⁻¹² and selective catalytic reduction (SCR) reactions of sulfur oxides have been employed to reduce the severity of SO_2 on the environment.¹³ Adsorption technology has also been used extensively for the removal of sulfur oxides.¹⁴⁻¹⁶ There have been significant investigations on the interaction of SO_2 with transition metal oxide surfaces, for instance, $\text{ZnO}(0001)$,¹⁷ $\text{Fe}_3\text{O}_4(100)$,¹⁸ MgO ,^{19,120} $\text{Cr}_2\text{O}_3(0001)$,¹⁹ and $\text{TiO}_2(110)$.²¹ Other traditional adsorbents like porous carbons²²⁻²⁴ and zeolites²⁵⁻²⁸ have also been extensively investigated for SO_2 capture and removal. However, due to their large pore size distribution and weakly binding sites, porous carbons material exhibit low selectivity towards SO_2 .

Two-dimensional (2D) layered materials are attractive alternatives to porous carbon materials for SO_x removal because of their large specific surface areas and highly exposed reactive active sites for adsorption. Various 2D materials such as MXenes,²⁸ graphene,²⁹ silicene,³⁰ graphene oxide,³¹⁻³⁵ and monolayer InN ,³⁶ have been widely investigated for SO_x gas sensing and trapping. The

application of graphene-like MoS₂ monolayer in heterogeneous catalysis and gas adsorption has also attracted a great deal of research attention lately.^{37,38} Like MoS₂, layered iron (II) sulfide (FeS) has emerged as a novel material for environmental and catalytic applications due of its germane electronic properties and high surface reactivity.³⁹⁻⁴³ Earlier investigations have shown that FeS exhibits strong catalytic activity towards major environmental pollutants such as nitrogen oxide (NO₂),⁴² and carbon dioxide (CO₂).⁴¹ There also exist reports on the adsorption and the direct desulfurization mechanisms of organosulfur compounds such as thiophene (C₄H₄S) on FeS nanocatalyst, with favourable thermodynamics and kinetics predicted for the scission of the C–S bonds.⁴³ A plasma-assisted catalytic reduction of SO₂ to elemental sulfur has been demonstrated over supported iron sulfide catalysts (FeS and FeS₂), which dramatically promotes low-temperature reduction of SO₂ by 148–200%, with over 98% selectivity to elemental sulfur.⁴⁴ ⁴⁵ Although the surface chemistry of a catalyst directly influences the catalytic performance, there exists limited reports dedicated to the characterizing surface structures and composition of FeS, and subsequently unravelling adsorption and dissociation mechanisms of SO_x on the FeS surfaces.

Knowledge of the initial adsorption geometries and the subsequent dissociation mechanism of SO_x on the different surfaces of FeS will provide a deeper understanding of the reactivity of organosulfur compounds. Notwithstanding, the determination of the lowest-energy adsorption geometries of SO_x at FeS surfaces is limited and the physical factors that dictate the adsorption remain poorly understood at the atomic level. In present work, we have performed a comprehensive first-principles density functional theory calculations to provide detailed molecular-level insights into the adsorption and dissociation mechanism of SO_x at FeS (001), (011), and (111) surfaces. The energetically most favourable adsorption geometries and adsorption sites of SO₂ and SO₃ at the FeS surfaces are predicted and the corresponding structural parameters are systematically characterized. Partial density of states (PDOS), differential charge

density, and vibrational frequency analyses were carried out to provide molecular-level insights into the bonding mechanism of SO_x on the FeS surfaces. Finally, the reaction energies and activation barriers for the dissociation of SO_2 on the reactive FeS (011) and (111) surface are presented and discussed.

2. COMPUTATIONAL DETAILS

All calculations to determine the lowest-energy adsorption geometries and their energetics were carried out within the Vienna Ab-initio Simulation Package (VASP).^{46,47} The electronic exchange-correlation potentials were described using the generalized gradient approximation of Perdew, Burke, and Ernzerhof (GGA-PBE) functional.^{48,49} Dispersion forces were accounted for in our calculations via the Grimme's DFT-D3 scheme.⁵⁰ The energy cut-off for the plane-waves was set 500 eV, which convergences the total energy of the SO_x -FeS systems to within 10^{-6} eV. The conjugate gradient minimization algorithm was employed for geometry optimizations, ensuring that the forces on each relaxed atom reached 0.01 eV/Å. A $11 \times 11 \times 9$ and $5 \times 5 \times 1$ Monkhorst-Pack⁵¹ k -point meshes were used to sample the Brillouin zone of the bulk and surfaces of FeS, respectively.

Mackinawite (FeS) was modelled in the tetragonal structure (space group, $P4/nmm$)⁵²⁻⁵⁵ as shown in **Figure 1**. Full geometry optimization predicts the lattice constants at $a = b = 3.615$ Å, $c = 5.001$ Å, in good agreement with known experimental⁵²⁻⁵⁴ and previous theoretical studies (See Table S1, Supplementary Information).^{42,55-57} The commonly expressed growth facets in FeS nanocrystals^{42,57} (*i.e.*, (001), (011), and (111) surfaces) were employed for the characterization of SO_x adsorption and dissociation mechanisms. A vacuum size of 15 Å was introduced in the c -direction to avoid interactions between periodic slabs. To ensure the prediction of reliable adsorption energies for the isolated SO_x species, large surface areas ((3×3) , (3×2) , and (3×2) supercells for the (001), (011), and (111) surface, respectively) were considered (Figure 2). The

strength of $\text{SO}_x\text{-FeS}$ interactions was characterized by the adsorption energy, calculated using the equation: $E_{\text{ads}} = E_{\text{surface+SO}_x} - (E_{\text{surface}} + E_{\text{SO}_x})$, where $E_{\text{surface+SO}_x}$, E_{surface} , and E_{SO_x} are the total energy of the combined FeS- SO_x system, the isolated FeS surface, and the isolated SO_x molecule, respectively. Charge transfers between the FeS surfaces and SO_x molecules was quantified via Bader charge analyses.⁵⁸ Transition state (TS) structures were located using the climbing-image nudged elastic band (CI-NEB) method⁵⁹ and confirmed via vibrational frequency calculations.

3. RESULTS AND DISCUSSIONS

3.1 SO_2 Adsorption at FeS (001), (011) and (111) Surfaces

In the gas-phase, SO_2 has a bent structure with S–O bond length of 1.431 Å and the $\alpha(\text{OSO})$ angle of 119.0°.^{60,61} The optimized S–O bond length 1.454 Å and $\alpha(\text{OSO})$ angle of 119.3° compare closely with the experimental⁶¹ and previous theoretical^{62–66} gas phase results. Different initial adsorption possibilities of SO_2 at the FeS (001), (011) and (111) surfaces have been considered in order to determine the most-stable adsorption geometries. The FeS- SO_x coordination is denoted as $\eta_y^x(m,n)$, wherein x represents the number of interacting SO_x atoms, y represents number surface binding sites, m and n in the bracket denotes the specific interacting atoms of SO_x . For example, the notation $\eta_2^2(\text{S},\text{O})$ indicates that two SO_x atoms (S and O) interact with two different surface binding sites (if at Fe-sites, then it forms one Fe–O bond and one Fe–S bond). The FeS(001) surface is found to be the least reactive surface towards SO_2 adsorption, as the molecule physisorbed at all binding sites and binding geometries (**Figure 3a1**), releasing adsorption energy of –0.24 eV. Consistent with the weak adsorption, no significant charge redistribution within the $\text{SO}_2\text{-FeS}(001)$ complex was found (**Figure 3a2**), and a negligible charge transfer of 0.08 e^- is calculated.

Unlike the FeS(001) surface, the SO₂ molecule chemisorbs strongly at the Fe sites on the FeS(011) surface as shown in **Figure 4**. The SO₂ molecule can be adsorbed in a tridentate coordination configuration with all three atoms interacting with two surface iron sites (denoted as $\eta_2^3(\text{S,O,O})$), bidentate configurations with either two Fe–O bonds (denoted as $\eta_2^2(\text{O,O})$) or with one Fe–O bond and one Fe–S bond (denoted $\eta_2^2(\text{S,O})$) or a monodentate configuration *via* a single Fe–O bond (denoted $\eta_1^1(\text{O})$). The most stable configuration is calculated to be a tridentate $\eta_2^3(\text{S,O,O})$ configuration (**Figure 4a**), with an adsorption energy of –2.18 eV. The adsorption energies of the bidentate $\eta_2^2(\text{O,O})$, $\eta_2^2(\text{S,O})$, and monodentate $\eta_1^1(\text{O})$ configurations on the other hand are calculated at –1.99, –1.77, and –1.29 eV, respectively. In the lowest-energy tridentate $\eta_2^3(\text{S,O,O})$ configuration (**Figure 4a**), the interacting S–Fe bond is predicted at 2.342 Å, whereas the two O–Fe bonds are predicted at 2.005 and 1.949 Å. For the $\eta_2^2(\text{O,O})$ configuration (**Figure 4b**), the two O–Fe bonds are predicted at 1.928 and 1.940 Å, and for the $\eta_2^2(\text{S,O})$ configuration (**Figure 4c**), the S–Fe and O–Fe bonds are respectively calculated at 2.087 and 1.971 Å. For the monodentate $\eta_1^1(\text{O})$ configuration (**Figure 4d**), the O–Fe bond is obtained at 1.849 Å.

In all four adsorption configurations, the adsorption process lengthens the S–O bonds and contracts the $\alpha(\text{OSO})$ angle relative to the gas-phase SO₂ molecule as confirmed by vibrational frequencies analyses (**Table 1**). For instance, in the lowest-energy tridentate $\eta_2^3(\text{S,O,O})$ configuration (**Figure 4a**), the two S–O bonds are calculated at 1.568 Å and 1.547 Å, compared with the gas-phase bond length of 1.454 Å, and the intramolecular $\alpha(\text{OSO})$ angle reduced from 119.0 in the gas-phase to 113.0° in the adsorbed state. Elongation of the S–O bond distances have been reported in many earlier theoretical and experimental works on metallic^{62,65-69} and metal oxide⁷⁰⁻⁷³ surfaces. In all four chemisorbed configurations at the FeS(011) surface, the asymmetric (ν_{as}) and symmetric (ν_s) vibrational modes of SO₂ were significantly red-shifted

compared to the gas-phase SO₂ molecule (v_{as} = 1277 and v_s = 1087 cm⁻¹). For instance, in the most stable η_2^3 (S,O,O) configuration, the v_{as} and v_s are predicted at 915 and 812 cm⁻¹, which are much lower than that gas-phase values, confirmation their elongation and activation (**Table 1**).

Similar to the FeS(011) surface, a strong adsorption is predicted for SO₂ at the FeS(111) surface (**Figure 5** and **Table 1**). In the lowest-energy η_2^1 (S) adsorption geometry (**Figure 5a**), SO₂ binds via the S atom at Fe–Fe bridge site, releasing an adsorption energy of -2.15 eV. The other coordination geometries: η_2^2 (S,O), η_2^2 (O,O), and η_2^1 (O) (**Figure 5b-d**) released adsorption energies of -1.78 eV, -1.54 eV, and -1.24 eV, respectively. The interacting S–Fe bond in the most stable η_2^1 (S) coordination geometry is predicted at 2.176 Å (**Figure 5a**). In the η_2^2 (S,O) configuration (**Figure 5b**), the S–Fe and O–Fe bond distances are respectively predicted at 2.155 and 2.009 Å. For the bidentate η_2^2 (O,O) configuration (**Figure 5c**), the average O–Fe bond distance is obtained at 2.008 Å, whereas for the monodentate η_2^1 (O) configuration (**Figure 5d**), the O–Fe bond is 1.928 Å. Due to the strong interaction of the SO₂ molecule with the FeS(111) surface, an elongation in the S–O bonds and a decrease in the α (OSO) angle is observed in all adsorption geometries as shown in **Table 1**. The largest elongation in the S–O bond is calculated for the η_2^1 (O) geometry at 1.649 Å, compared to that of the η_2^1 (S), η_2^2 (S,O), and η_2^2 (O,O) geometries, which are calculated at 1.473 Å, 1.534 Å, and 1.518 Å, respectively, (**Figure 5**, **Table 1**). Consistently, the v_{as} and v_s vibration frequencies of SO₂ were significantly red-shifted relative to the gas-phase molecule (**Table 1**). The (v_{as} , v_s) of SO₂ adsorbed in the η_2^1 (S), η_2^2 (S,O), η_2^2 (O,O), and η_2^1 (O) configurations are predicted at (1202, 1028 cm⁻¹), (1163, 890 cm⁻¹), (1011, 889 cm⁻¹), and (1119, 569 cm⁻¹), respectively, compared to gas-phase SO₂ (1277, 1087 cm⁻¹).

Because of its high electron affinity of 1.1 eV,^{74,75} SO₂ act as an electron acceptor when it binds to metallic surfaces.^{62,65-69} At pure metal surfaces, the metal–SO₂ bonds occur through the

hybridization of the SO_x π^* -orbital with the d_z^2 surface orbital, giving rise to a charge transfer from the interacting surface species to the SO_2 molecule.^{66, 76,77} To gain insights into the charge transfer processes within the FeS– SO_2 systems, we have carried out Bader population analyses of the adsorbate atoms and the interacting surface species for all stable adsorption geometries. Due to physisorption at the FeS(001) surface, no charge transfers was observed (**Figure 3a**). However, due to SO_2 chemisorption at the (011) and (111) FeS surfaces, large charge transfers occurred from the surface to the adsorbing SO_2 (**Table 1**). The net charge gained by the SO_2 molecule when adsorbed at Fe sites on the FeS(011) surface via the $\eta_2^3(\text{S},\text{O},\text{O})$, $\eta_2^2(\text{O},\text{O})$, $\eta_2^2(\text{S},\text{O})$ and $\eta_1^1(\text{O})$ coordination geometries are calculated at 0.79, 0.72, 0.66, and 0.51 e^- , respectively (**Table 1**). Comparably, when adsorbed at the FeS(111) surface in the $\eta_2^1(\text{S})$, $\eta_2^2(\text{S},\text{O})$, $\eta_2^2(\text{O},\text{O})$, and $\eta_2^1(\text{O})$ coordination geometries, a net charge of 0.80, 0.68, 0.57, and 0.53 e^- were gained by the SO_2 molecule. The amount of charge transferred to the adsorbed SO_2 is found to dictate the binding energetics, with higher charge transfers leading to stronger adsorption. The geometrical changes observed in the SO_2 molecule upon adsorption (*i.e.*, elongation of S–O bonds and contraction in the $\alpha(\text{OSO})$ angles) can be attributed the higher charge gained. Differential charge density ($\Delta\rho = \rho_{\text{surface}+\text{SO}_2} - (\rho_{\text{surface}} + \rho_{\text{SO}_2})$) iso-surface contours analyses,⁷⁸⁻⁸⁰ provide further insights into electron density redistribution within the FeS– SO_x systems (**Figure 6(a1 & b1)**). A significant charge density accumulation (green contours) in the centers of the newly formed bonds is observed, which is consistent with SO_2 chemisorption. Besides, a strong hybridization between the SO_2 molecule and the interacting surface Fe atoms was observed (**Figure 6 (a2 & b2)**).

3.2 SO_3 Adsorption FeS (001), (011) and (111) Surfaces

The S–O bond length and $\alpha(\text{OSO})$ angle of gas-phase SO_3 are calculated at 1.435 Å and 120.0° in good agreement with experimental⁸¹ and previous theoretical^{82,83} results. Different initial adsorption possibilities of SO_3 were subjected to energy minimization in order to determine the

most-stable adsorption geometries at the (001), (011) and (111) FeS surfaces. Like SO₂, the SO₃ molecule is only physisorbed at the FeS(001) surface (**Figure 3b1**), releasing an adsorption energy of -0.51 eV. A shorter $S_{\text{mol}}-S_{\text{surf}}$ distance is calculated for SO₃ adsorption (2.544 Å) compared to SO₂ adsorption (3.225 Å) at the FeS(001) surface. This rise to small charge transfer of 0.17 e⁻ from the surface species to the adsorbing SO₃, resulting from electron density redistribution within the SO₃-FeS(001) as shown in **Figure 3b2**. For the SO₃-FeS(011) adsorption systems, the lowest-energy configuration was calculated to possess a $\eta_2^2(\text{O},\text{O})$ coordination (**Figure 7a**), with the SO₃ molecule interacting with the surface *via* two O-Fe bonds of average length 1.855 Å. This configuration released an adsorption energy of -3.03 eV, which is larger than the adsorption energies of the bidentate $\eta_2^2(\text{S},\text{O})$, and $\eta_1^2(\text{O},\text{O})$, and the monodentate $\eta_1^1(\text{O})$ configurations (**Figure 7(b-d)**), which are calculated at -2.68 eV, -1.83 eV, and -1.29 eV, respectively. It can be seen from the optimized geometrical parameters listed in **Table 2** and displayed in **Figure 7**, that the S-O bond distances become elongated and the $\alpha(\text{OSO})$ angle smaller compared to the gas-phase SO₃ geometry. In the case of the lowest-energy $\eta_2^2(\text{O}, \text{O})$ geometry (**Figure 7a**), the surface-bound S-O bonds and $\alpha(\text{OSO})$ angle are calculated at 1.605 Å and 104.6° compared to the gas-phase geometry ($\text{S-O} = 1.435$ Å, $\alpha(\text{OSO}) = 120^\circ$).

The optimized adsorption geometries of SO₃ at the FeS(111) surface are displayed in **Figure 8(a-c)**, whereas the calculated adsorption energetics and optimized geometrical parameters are reported in **Table 2**. The most favourable adsorption ($E_{\text{ads}} = -3.17$ eV) was calculated for the $\eta_2^1(\text{O})$ coordination geometry (**Figure 8a**), in which the SO₃ molecule binds through only one oxygen atom at a bridge Fe-Fe site. The strong adsorption promoted the dissociation of the surface bound S-O bond ($\text{SO}_3 \rightarrow \text{SO}_2 + \text{O}$), which is elongated to 2.444 Å, compared to 1.460 Å and 1.460 Å in the SO₂ fragment. When adsorbed in the $\eta_2^3(\text{S},\text{O},\text{O})$ and $\eta_2^2(\text{O},\text{O})$ coordination geometries (**Figure 8(b & c)**), the adsorption energies are calculated at -2.15

eV and -1.91 eV, respectively. These results suggest that on a normal FeS(111) surface, the SO_3 molecule will preferentially exist in a dissociated state.

Owing to its higher electron affinity (1.7 eV), higher charge transfers and larger adsorption energies are calculated for SO_3 compared to SO_2 (electron affinity = 1.1).^{74,75} This can be seen when comparing the increased charge donation from the FeS surfaces to adsorbing SO_3 than SO_2 as revealed by Bader population analysis (**Tables 1 and 2**). The charge gained by SO_3 when adsorbed in the most-stable adsorption geometries at the (011) and (111) surfaces was calculated at 1.10 e^- and 1.23 e^- , respectively, compared to 0.74 e^- and 0.80 e^- calculated for the most-stable SO_2 adsorption geometries at the (011) and (111) surfaces. Due to the strong charge gained by SO_3 , the S–O bond distances are predicted to be elongated relative to the gas-phase geometry (**Table 2**). It is obvious that the charge transfers from the FeS(111) surface to the both SO_3 and SO_2 adsorbates is more than that from the FeS(011) surface, which explains the stronger chemisorption of both species at the (111) surface than at the (011) surface. Analyses of the differential charge density iso-surface contour plots reveal strong electron density redistribution and accumulation within the bonding regions of the newly formed bonds, which is very much what one would expect for chemisorption (**Figure 9(a1 & b1)**). The partial density of states analyses (**Figure 9(a2 & b2)**) reveal strong hybridization especially between the O p -orbitals of the SO_2 molecule and the d -orbitals of the interacting surface Fe atoms.

3.3 Dissociation Mechanism of SO_2 and SO_3 at FeS (011) and (111) Surfaces

The optimized SO_2 adsorption geometries at the FeS (011) and (111) surfaces reveal significant activation of the S–O bonds, suggesting that these molecular species are probable precursors for SO_2 dissociation. Thus, the dissociation energetics (reaction energy (E^{rxn}) and activation energy barrier (E^{a})) of SO_2 at the FeS (011) and (111) surfaces (*i.e.*, $\text{SO}_2 \rightarrow \text{SO} + \text{O}$) has been investigated. The reaction profile for SO_2 dissociation to $\text{SO}+\text{O}$ fragments at the (011) and (111)

FeS surfaces are shown in **Figure 10** and **Figure 11**, respectively. The S–O bond dissociation of is predicted to be endothermic by 0.82 eV with an activation barrier of 1.21 eV at the (011) surface (**Figure 10**). In the transition state structure, the dissociating S---O bond was calculated at 2.120 compared to 3.611 Å for the fully dissociated S–O bond. The S–Fe and O–Fe distances in the fully dissociated SO and O fragments is predicted at 1.985 and 1.623 Å, respectively. In contrast, the dissociation of the S–O bond at the FeS(111) surface is predicted to be highly exothermic ($E^{\text{rxn}} = -1.89$ eV) with an activation barrier of 1.37 eV (**Figure 11**). The fully dissociated structure showed the SO and O fragments adsorb at bridge-Fe sites with the average S–Fe and O–Fe bonds calculated at 2.133 Å and 1.751 Å. The favourable thermodynamics for the dissociation of SO₂ at the (111) surface coupled with the low activation energy barrier suggest that the FeS(111) surface will not only strongly adsorb the SO₂ molecules but further convert it other sulfur-containing species of lower risk. Compared to SO₂, a spontaneous dissociation of SO₃ is observed at the FeS(111) surface due to the strong adsorption (**Figure 8a**). At the FeS(011), the dissociation of one of the S–O bonds is predicted to be exothermic by 0.28 eV with an activation barrier of 1.31 eV as shown in **Figure 12**. In the fully dissociated state, the SO₂ and O fragments remained adsorbed at Fe-sites. Further dissociation of the SO₂ fragment in the presence of the atomic O is expected to result in the formation of SO and O₂ molecule.

4. SUMMARY AND CONCLUSIONS

We have systematically investigated the surface chemistries of sulfur oxides (SO₂, and SO₃) adsorbed on the low-index FeS (001), (011), and (111) surfaces using the dispersion-corrected density functional theory (DFT-D3) methodology. Overall, SO₃ is demonstrated to exhibit stronger reactivity than SO₂ towards the different FeS surfaces preferentially at the Fe sites. The lowest-energy adsorption geometry for SO₂ and SO₃ on FeS(011) surface is predicted to be η_2^3 (S,O,O) and η_2^2 (O,O), respectively, whereas on the (111) surface, they are predicted to

coordinate in the $\eta_2^1(\text{S})$ and $\eta_2^1(\text{O})$ geometry, respectively. The adsorption process is demonstrated to be driven by a strong charge transfers from the FeS surface to the adsorbing SO_x species, which resulted in their significant structural changes (elongated S–O bond and $\alpha(\text{OSO})$ reduction), confirmed by Bader charge and vibration frequency analyses. The FeS(111) surface is shown to display stronger catalytic activity towards SO₂ adsorption and dissociation than the FeS(011) surface with favourable thermodynamics and kinetics. We believe that the molecular-level insights obtained from the present study will be useful in the design of novel iron sulfide nanocatalysts for the removal SO_x or converting them to lower-risk sulfur-containing species.

ACKNOWLEDGEMENTS

NYD acknowledges the UK Engineering and Physical Sciences Research Council (EPSRC) for funding (Grant EP/S001395/1). We also acknowledge the support of the African University of Science and Technology and the John and Willie Leone Family Department of Energy and Mineral Engineering of the Pennsylvania State University. Computer simulations for this work were performed on the Roar Supercomputer of the Pennsylvania State University.

AUTHOR DECLARATIONS

Conflict of Interest: The authors have no conflicts to disclose.

REFERENCES

1. L. Yao, O. Garmash, F. Bianchi, J. Zheng, C. Yan, J. Kontkanen, H. Junninen, S.B. Mazon, M. Ehn, P. Paasonen, M. Sipilä, M. Wang, X. Wang, S. Xiao, H. Chen, Y. Lu, B. Zhang, D. Wang, Q. Fu, F. Geng, L. Li, H. Wang, L. Qiao, X. Yang, J. Chen, V.-M. Kerminen, T. Petäjä, D.R. Worsnop, M. Kulmala, L. Wang, *Science*, **361**, 278–281 (2018).
2. T.F. Berglen, T.K. Berntsen, I.S.A. Isaksen, J.K. Sundet, *J. Geophys. Res.: Atmos.*, **109**, D19310 (2004).
3. T. Hussain, T. Kaewmaraya, S. Chakraborty, R. Ahuja, *J. Phys. Chem. C.*, **120**, 25256–25262 (2016).
4. R. Li, X. Kou, J. Tian, Z. Meng, Z. Cai, F. Cheng, C. Dong, *Chemosphere*, **112**, 296–304 (2014).
5. J. G. Calvert, A. Lazrus, G. L. Kok, B. G. Heikes, J. G. Walega, J. Lind, C. A. Cantrell, *Nature*, **317**, 27–35 (1985).
6. M.F. Ruiz-Lopez, M.T.C. Martins-Costa, J.M. Anglada, J.S. Francisco, *J. Am. Chem. Soc.* **141**, 16564–16568 (2019).
7. E. Wigenstama, L. Elfsmarka, A. Buchta, S. Jonasson, *Toxicology*, **368**–369, 28–36 (2016).
8. M. Guarnieri, J.R. Balmes, *Lancet*, **383**, 1581–1592 (2014).
9. U.S. Environmental Protection Agency. Review of the Primary National Ambient Air Quality Standards for Sulfur Oxides. Federal Register, Vol. 83, No. 111, Proposed Rules 26753 (2018).
10. Z. Zhao, Y. Zhang, W. Gao, J. Baleta, C. Liu, W. Li, W. Weng, H. Dai, C. Zheng, X. Gao, *Process Safety and Environmental Protection*, **150**, 453–463 (2021).
11. Y. Gong, Z.-G. Yang, *Fuel Process. Technol.* **181**, 279–293 (2018).
12. C. Zheng, Y. Wang, Y. Liu, Z. Yang, R. Qu, D. Ye, C. Liang, S. Liu, X. Gao, *Fuel*. **241**, 327–346 (2019).
13. S. E. Mousavi, H. Pahlavanzadeh, M. Khani, H. A. Ebrahim, A. Mozaffari, *Reac Kinet Mech Cat*, **124**, 669–682 (2018).
14. H. Wang, R. Hao, M. Gao, Z. Zhang, Z. Hao, *Processes*, **9**, 325 (2021).
15. H-H. Tseng, M.-Y. Wey, *Carbon*, **42**, 2269–2278 (2004).

16. S. Wang, S. Xu, S. Gao, P. Xiao, M. Jiang, H. Zhao, B. Huang, L. Liu, H. Niu, J. Wang, D. Guo, *Scientific Reports*, **11**, 11003 (2021).
17. A. Önsten, D. Stoltz, P. Palmgren, S. Yu, T. Claesson, M. Göthelid, U.O. Karlsson, *Surf. Sci.*, **2013**, 608, 31-43
18. D. Stoltz, A. Önsten, U.O. Karlsson, M. Göthelid, *Appl. Phys. Lett.*, **91**, 093107 (2007).
19. J.A. Rodriguez, T. Jirsak, M. Pérez, S. Chaturvedi, M. Kuhn, L. González, A. Maiti, *Am. Chem. Soc.*, **122**, 12362–12370 (2000).
20. H. Wang, C. Zhong, Q. Ma, J. Ma, H. He, *Environ. Sci.: Nano*, **7**, 1092-1101 (2020).
21. E. Román, J. de Segovia, J. Martín-Gago, G. Comtet, L. Hellner, *Proceedings of the 5th Eur. Vacuum Conference*, **48**, 597-600 (1997).
22. H. Yi, Z. Wang, H. Liu, X. Tang, D. Ma, S. Zhao, B. Zhang, F. Gao, Y. Zuo, *J. Chem. Eng. Data*, **59**, 1556–1563 (2014).
23. J. H. Zhang, P. X. Zhang, M. Y. Li, Z. W. Shan, J. Wang, Q. Deng, Z. L. Zeng, S. G. Deng, *Ind. Eng. Chem. Res.*, **58**, 14929–14937 (2019).
24. P. Davini, *Carbon*, **28**, 565–571 (1990).
25. I. Matito-Martos, A. Martin-Calvo, J. J. Gutierrez-Sevillano, M. Haranczyk, M. Doblare, J. B. Parra C. O. Ania, S. Calero, *Phys. Chem. Chem. Phys.* **16**, 19884–19893 (2014).
26. A. Srinivasan, M. W. Grutzeck, *Environ. Sci. Technol.* **33**, 1464–1469 (1999).
27. H. H. Yi, H. Deng, X. L. Tang, Q. F. Yu, X. Zhou, H. Y. Liu, *J. Hazard. Mater.*, **203**, 111–117 (2012).
28. S. Ma, D. Yuan, Z. Jiao, T. Wang, X. Dai, *J. Phys. Chem. C.*, **121**, 24077-24084 (2017).
29. X.-Y. Liu, J.-M. Zhang, K.-W. Xu, V. Ji, *Appl. Surf. Sci.*, **313**, 405–410 (2014).
30. T. Hussain, T. Kaewmaraya, S. Chakraborty, R. Ahuja, *J. Phys. Chem. C.*, **120**, 25256–25262 (2016).
31. D.J. Babu, F.G. Kuhl, S. Yadav, D. Markert, M. Bruns, M.J. Hampe, J.J. Schneider, *RSC Adv.*, **6**, 36834-36839 (2016).
32. H. Zhang, W. Cen, J. Liu, J. Guo, H. Yin, P. Ning, *Appl. Surf. Sci.*, **324**, 61-67 (2015).
33. M. Seredych, T.J. Bandoz, *J. Phys. Chem. C*, **114**, 14552-14560 (2010).
34. L. Shao, G. Chen, H. Ye, Y. Wu, Z. Qiao, Y. Zhu, H. Niu, *Eur. Phys. J. B*, **86**, 54 (2013).
35. C. Chen, K. Xu, X. Ji, L. Miao, J. Jiang, *Phys. Chem. Chem. Phys.* **16**, 11031-11036 (2014).
36. X. Sun, Q. Yang, R. Meng, C. Tan, Q. Liang, J. Jiang, H. Ye, X. Chen, *Appl. Surf. Sci.*, **404**, 291–299 (2017)
37. D. Ma, W. Ju, T. Li, X. Zhang, C. He, B. Ma, Z. Lu, Z. Yang, *Appl. Surf. Sci.*, **383**, 98–105 (2016).
38. J. Zhu, H. Zhang, Y. Tong, L. Zhao, Y. Zhang, Y. Qiu, X. Lin, *Appl. Surf. Sci.*, **419**, 522–530 (2017).
39. Y. Gong, J. Tang, D. Zhao, *Water Res.*, **89**, 309–320 (2016).
40. R.E. Mielke, K.J. Robinson, L.M. White, S.E. McGlynn, K. McEachern, R. Bhartia, I. Kanik, M.J. Russell, *Astrobiology*, **11**, 933–950 (2011).
41. N. Y. Dzade, A. Roldan, N. H. de Leeuw, *J. Chem. Phys.*, **143**, 094703 (2015).
42. N. Y. Dzade, A. Roldan, N. H. de Leeuw, *Phys. Chem. Chem. Phys.*, **16**, 15444–15456 (2014).
43. N.Y. Dzade, N.H. de Leeuw, *J. Phys. Chem. C.*, **122**, 359–370 (2018).
44. M.S. AlQahtani, X. Wang, J.L. Gray, S.D. Knecht, S.G. Bilén, C. Song, *Journal of Catalysis* **391**, 260–272 (2020).
45. M.S. AlQahtani, S.D. Knecht, X. Wang, S.G. Bilen, and C. Song, *ACS Catal.* **10**, 5272–5277 (2020).
46. G. Kresse, J. Furthmüller, *Comput. Mater. Sci.*, **6**, 15–50 (1996).
47. G.; Kresse, D. Joubert, *Phys. Rev. B: Condens. Matter Mater. Phys.*, **59**, 1758–1775 (1999).
48. J. P. Perdew, K. Burke, M. Ernzerhof, *Phys. Rev. Lett.*, **78**, 1396 (1997).
49. J. P. Perdew, K. Burke, M. Ernzerhof, *Phys. Rev. Lett.*, **77**, 3865–3868 (1996).
50. S. Grimme, J. Antony, S. Ehrlich, H. Krieg, *J. Chem. Phys.*, **132**, 154104 (2010).

51. H. J. Monkhorst, J. D. Pack, *Phys. Rev. B*, **13**, 5188–5192 (1976).
52. D. J. Vaughan, J. R. Craig, *Mineral Chemistry of Metal Sulfides*; Cambridge University Press: New York, **1978**.
53. A. R. Lennie, S. A. T. Redfern, P. F. Schofield, D. J. Vaughan, *Mineral. Mag.*, **59**, 677–683 (1995).
54. R. A. Berner, *Science*, **137**, 669 (1962).
55. A. Zivković, M. Somers, E. Camprubi, H.E. King, M. Wolthers, N.H. de Leeuw, *Catalysts*, **11**, 486 (2021).
56. A.J. Devey, R. Grau-Crespo, N.H. de Leeuw, *J. Phys. Chem C.*, **112**, 10960 (2008).
57. J. Brgoch, G. J. Miller, *J. Phys. Chem. A.*, **116**, 2234 (2012).
58. W. Tang, E. Sanville, G. Henkelman, *J. Phys. Condens. Matter.* **21**, 084204 (2009).
59. G. Mills, H. Jonsson, G. K. Schenter, *Surf. Sci.*, **324**, 305–337 (1995).
60. G. Herzberg, *Electronic spectra and electronic structure of polyatomic molecules*, Van Nostrand, New York, **1966**.
61. N.M. Galea, J.M.H. Lo, T.A. Ziegler, *Journal of Catalysis*, **263**, 380–389 (2009).
62. X. Chu, Z. Lu, Z. Yang, D. Ma, Y. Zhang, S. Li, P. Gao, *Physics Letters A*, **378**, 659–666 (2014).
63. W. F. Schneider, J. Li, K. C. Hass, *J. Phys. Chem. B.*, **105**, 6972–6979 (2001).
64. X. Lin, W.F. Schneider, B.L. Trout, *J. Phys. Chem. B*, **106**, 12575–12583 (2002).
65. Y. Sakai, M. Koyanagi, K. Mogi, E. Miyoshi, *Surf. Sci.*, **513**, 272–282 (2002).
66. R. Mozo, M. K. Augusta, M. M. Rahman, W. A. Diño, E. T. Rodulfo, H. Kasai, *J. Phys.: Condens. Matter*, **19**, 365244 (2007).
67. G. J. Jackson, D. P. Woodruff, A.S.Y. Chan, R. G. Jones, B.C.C. Cowie, *Surf. Sci.* **577**, 31–41 (2005).
68. G. Liu, J. A. Rodriguez, J. Dvorak, J. Hrbek, T. Jirsak, *Surf. Sci.*, **505**, 295 (2002).
69. Y. Mathieu, L. Tzanis, M. Souillard, J. Patarin, M. Vierling, M. Molière, *Fuel Processing Technology*, **114**, 81–100 (2013).
70. D. Langhammer, J. Kullgren, L. Österlund, *J. Am. Chem. Soc.*, **142**, 21767–21774 (2020).
71. J. Baltrusaitis, D.M. Cwiertny, V.H. Grassian, *Phys. Chem. Chem. Phys.*, **9**, 5542–5554 (2007).
72. J. A. Rodriguez, J. García, L. González, *Chem. Phys. Lett.*, **365**, 380 (2002).
73. E.W. Rothe, S.Y. Tang, G.P. Reck, *J. Chem. Phys.* **62**, 3829 (1975).
74. J.C. Rienstra-Kiracofe, G.S. Tschumper, H.F. Schaefer III, S. Nandi, G.B. Ellison, *Chem. Rev.*, **102**, 231–282 (2002).
75. S. Sakaki, H. Sato, Y. Imai, K. Morokuma, K. Ohkubo, *Inorg. Chem.* **24**, 4538–4544 (1985).
76. G. Pacchioni, A. Clotet, J. M. Ricart, *Surf. Sci.*, **315**, 337 (1994).
77. N. Y. Dzade, A. Roldan, N. H. de Leeuw, *J. Chem. Phys.* **139**, 124708 (2013).
78. N.Y. Dzade, *ACS Omega*, **5**, 1025–1032 (2020).
79. N.Y. Dzade, N.H. de Leeuw, *Catalysts*, **11**, 127 (2021).
80. V. Meyer, D. Sutter, H. Dreizler, *Z. Naturforsch.*, **46a**, 710–714 (1991).
81. W. F. Schneider, *J. Phys. Chem. B*, **108**, 1, 273–282 (2004).
82. R. Hummatov, O. Gülseren, E. Ozensoy, D. Toffoli, H. Üstünel, *J. Phys. Chem. C*, **116**, 6191–6199 (2012).
83. W.B. Person, G. Zerbi, *Vibrational Intensities in Infrared and Raman Spectroscopy*. ed. Elsevier, Amsterdam, **1982**.
84. T. Shimanouchi, *Tables of Molecular Vibrational Frequencies, Consolidated Volume 1*, NSRDS NBS-39, **1972**.

LIST OF TABLES

Table 1: Adsorption energy and structure parameters of SO₂ adsorbed on FeS (001), (011) and (111) surfaces. Δq denote net charge gained by the SO₂ molecule.

Surface	Configuration	E_{ads}/eV	$d(\text{S}-\text{O}_1)/\text{\AA}$	$d(\text{S}-\text{O}_2)/\text{\AA}$	$d(\text{S}-\text{Fe})/\text{\AA}$	$d(\text{O}-\text{Fe})/\text{\AA}$	$\alpha(\text{OSO})/^\circ$	$\Delta q/e$	$v_{\text{as}}, v_{\text{s}}(\text{S}-\text{O})\text{ cm}^{-1}$
	Free SO ₂	---	1.454 (1.431) ^a	1.454 (1.431) ^a	---	---	119.3 (119.0) ^a	0.00	1277, 1087 (1362, 1151) ^b
FeS(001)	physisorbed	-0.24	1.459	1.457	4.421	4.109	118.9	0.08	1259, 1068
FeS(011)	$\eta_2^3(\text{S}, \text{O}, \text{O})$	-2.18	1.568	1.547	2.342	2.005, 1.949	113.0	0.74	915, 812
	$\eta_2^2(\text{O}, \text{O})$	-1.99	1.545	1.543	---	1.928, 1.940	112.4	0.70	1121, 768
	$\eta_2^2(\text{S}, \text{O})$	-1.77	1.559	1.471	2.087	1.971	111.0	0.66	932, 801
	$\eta_1^1(\text{O})$	-1.29	1.536	1.400	---	1.849	113.5	0.51	923, 811
FeS(111)	$\eta_2^1(\text{S})$	-2.15	1.473	1.466	2.176	---	117.5	0.80	1202, 1028
	$\eta_2^2(\text{S}, \text{O})$	-1.78	1.534	1.464	2.155	2.009	113.8	0.68	1163, 890
	$\eta_2^2(\text{O}, \text{O})$	-1.54	1.518	1.516	---	2.008	108.2	0.57	1011, 889
	$\eta_2^1(\text{O})$	-1.24	1.649	1.476	---	1.928	109.3	0.53	1119, 569

^aReference 61; ^bReference 84

Table 2: Adsorption energy and structure parameters of SO₃ adsorbed on the FeS (001), (011) and (111) surfaces. Δq denote net charge gained by the SO₃ molecule.

Surface	Configuration	E _{ads} /eV	d(O–Fe) /Å	d(S–Fe) /Å	d(S–O) /Å	$\alpha(\text{OSO}) /^\circ$	Δq /e	$\nu(\text{S–O}_i) / \text{cm}^{-1}$
	Free SO ₃	---	---	---	1.442 (1.420) ^a	120.0 (120.0) ^a		1311, 1303, 989 (1391, 1391, 1065) ^b
FeS(001)	physisorbed	−0.51	3.708	3.983	1.449, 1.453, 1.450	119.0, 118.4, 119.5	0.17	1272, 1256, 967
FeS(011)	η_2^2 (O, O)	−3.03	1.855	---	1.605, 1.605, 1.476	104.6, 108.6, 107.8	1.10	1088, 661, 582
	η_2^2 (S, O)	−2.68	1.908	2.210	1.588, 1.468, 1.462	109.2, 109.1, 118.4	0.95	1182, 1028, 688
	η_1^2 (O, O)	−1.83	1.882	---	1.644, 1.640, 1.466	89.8, 109.9, 109.6	1.13	1093, 673, 595
	η_1^1 (O)	−1.29	1.849	---	1.566, 1.470, 1.470	110.5, 110.1, 119.4	0.72	1144, 975, 746
FeS(111)	η_2^1 (O)	−3.17	1.756	---	2.444, 1.460, 1.460	118.3	1.23	1248, 1073, 608
	η_2^3 (S, O, O)	−2.15	2.084	2.303	1.526, 1.518, 1.450	108.5, 116.5, 115.7	0.94	1209, 985, 858
	η_2^2 (O, O)	−1.91	1.872	---	1.586, 1.583, 1.466	101.1, 110.4, 110.3		1119, 715, 667

^aReference 81; ^bReference 85

LIST OF FIGURES

Figure 1: The layered structure of FeS with the tetragonal unit cell highlighted by dashed line. (Colour code: Fe = grey, S = yellow).

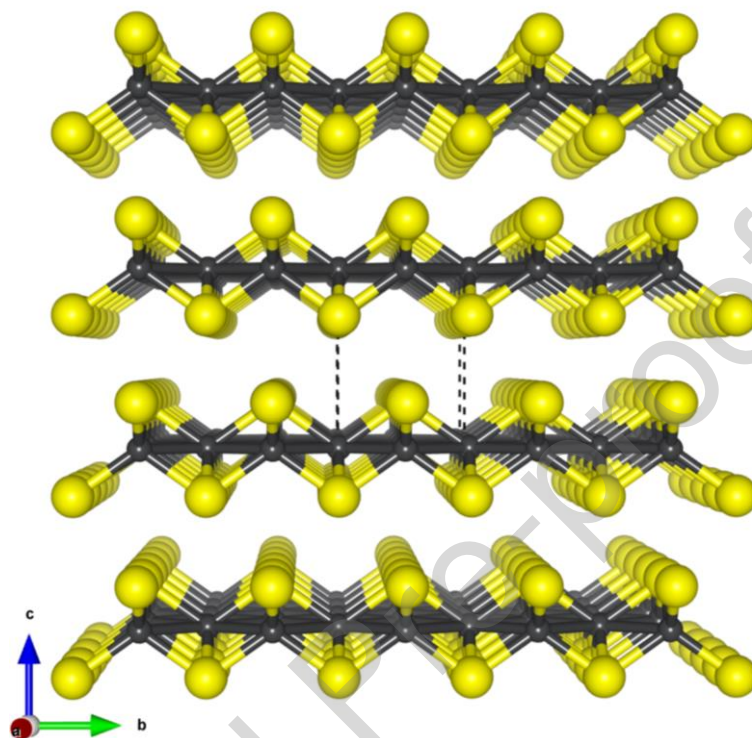


Figure 2: Optimized surface structures of the (a) FeS(001), (b) FeS(011), and FeS(111) surfaces, in side (top) and top (bottom) views, used for the SO_x adsorption characterization. (Colour scheme: Fe = grey, S = yellow).

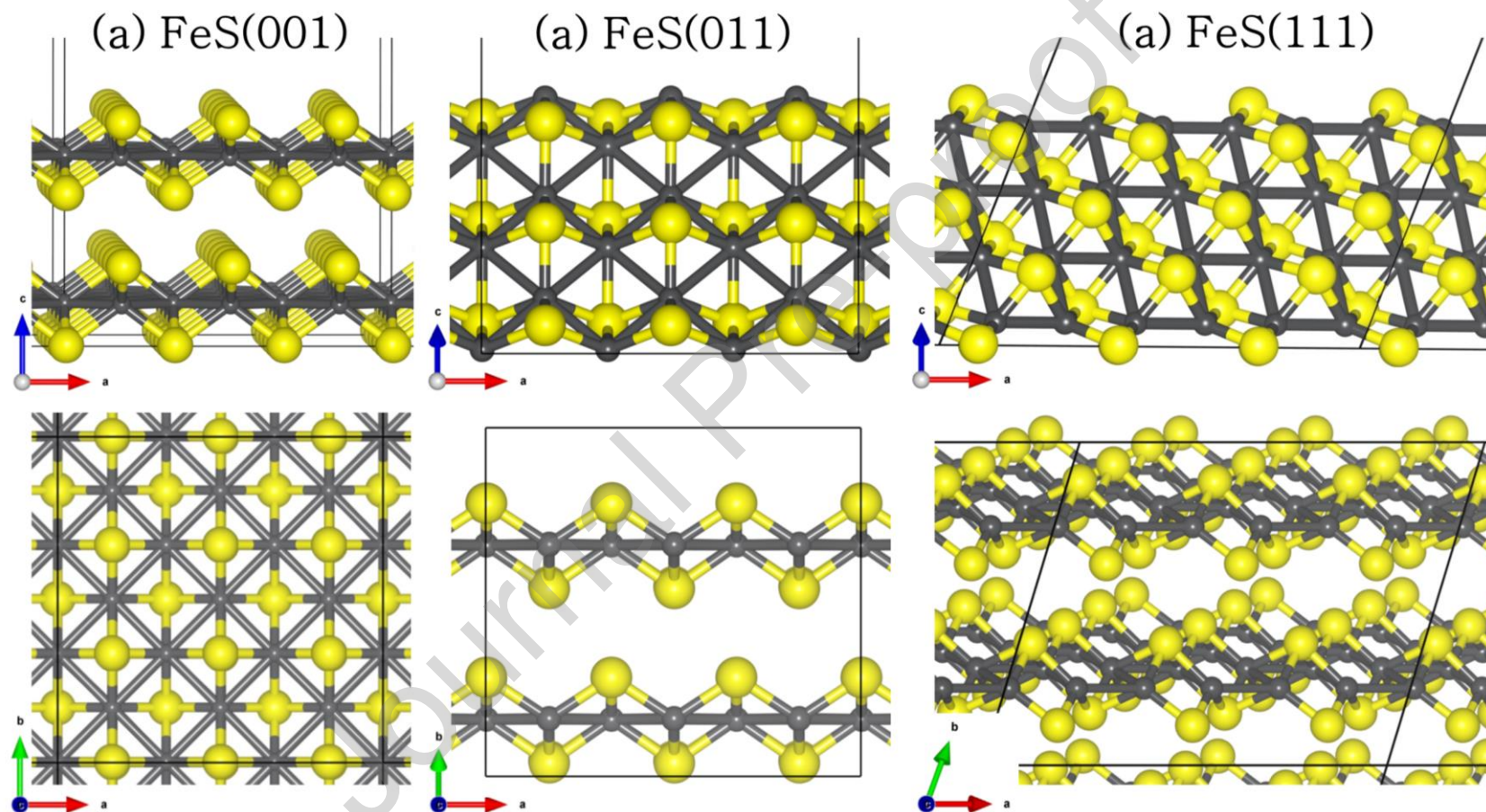


Figure 3: Optimized adsorption geometries of SO₂ and SO₃ (a1 & b1) on FeS (001) surface. The corresponding electron density difference isosurface contours upon their adsorption shown in (a2) and (b2), respectively. (Colour code: Fe = grey, S_{slab} = yellow, S_{molecule} = green, and O = red).

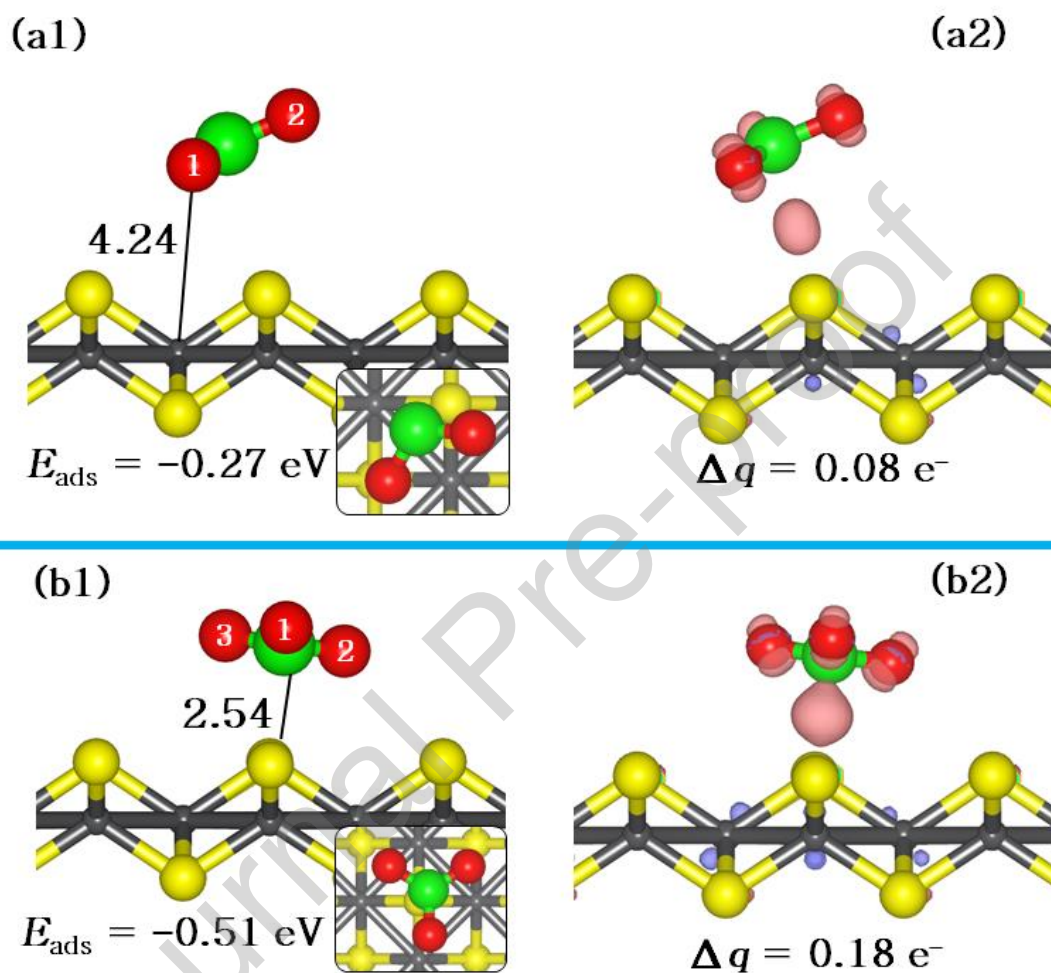


Figure 4: Optimized adsorption geometries of SO₂ on FeS (011) surface. The inserts show top views. (Colour code: Fe = grey, S_{slab} = yellow, S_{molecule} = green, and O = red).

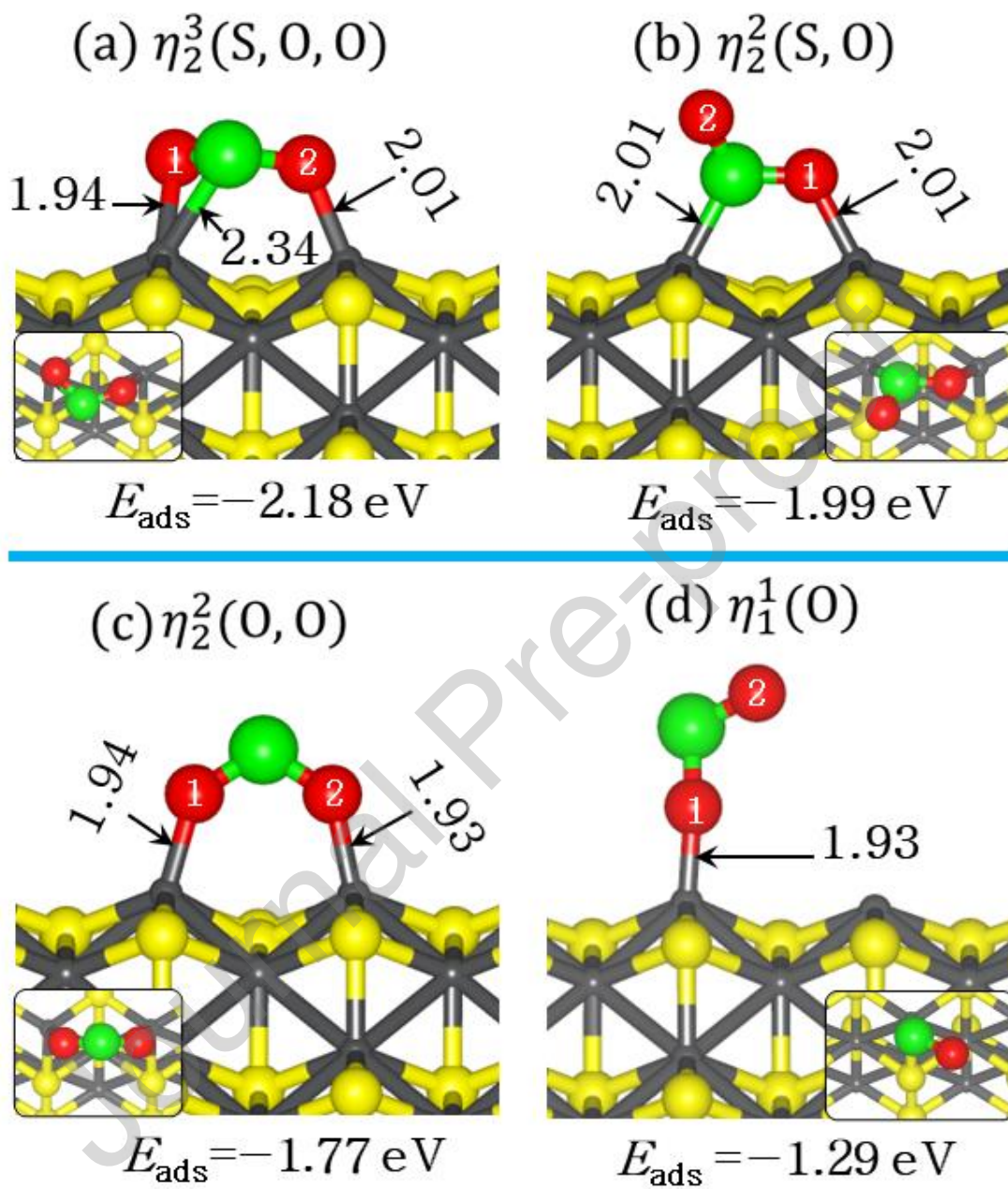


Figure 5: Optimized adsorption geometries of SO_2 on FeS (111) surface. The inserts show top views. (Colour code: Fe = grey, S_{slab} = yellow, $\text{S}_{\text{molecule}}$ = green, and O = red).

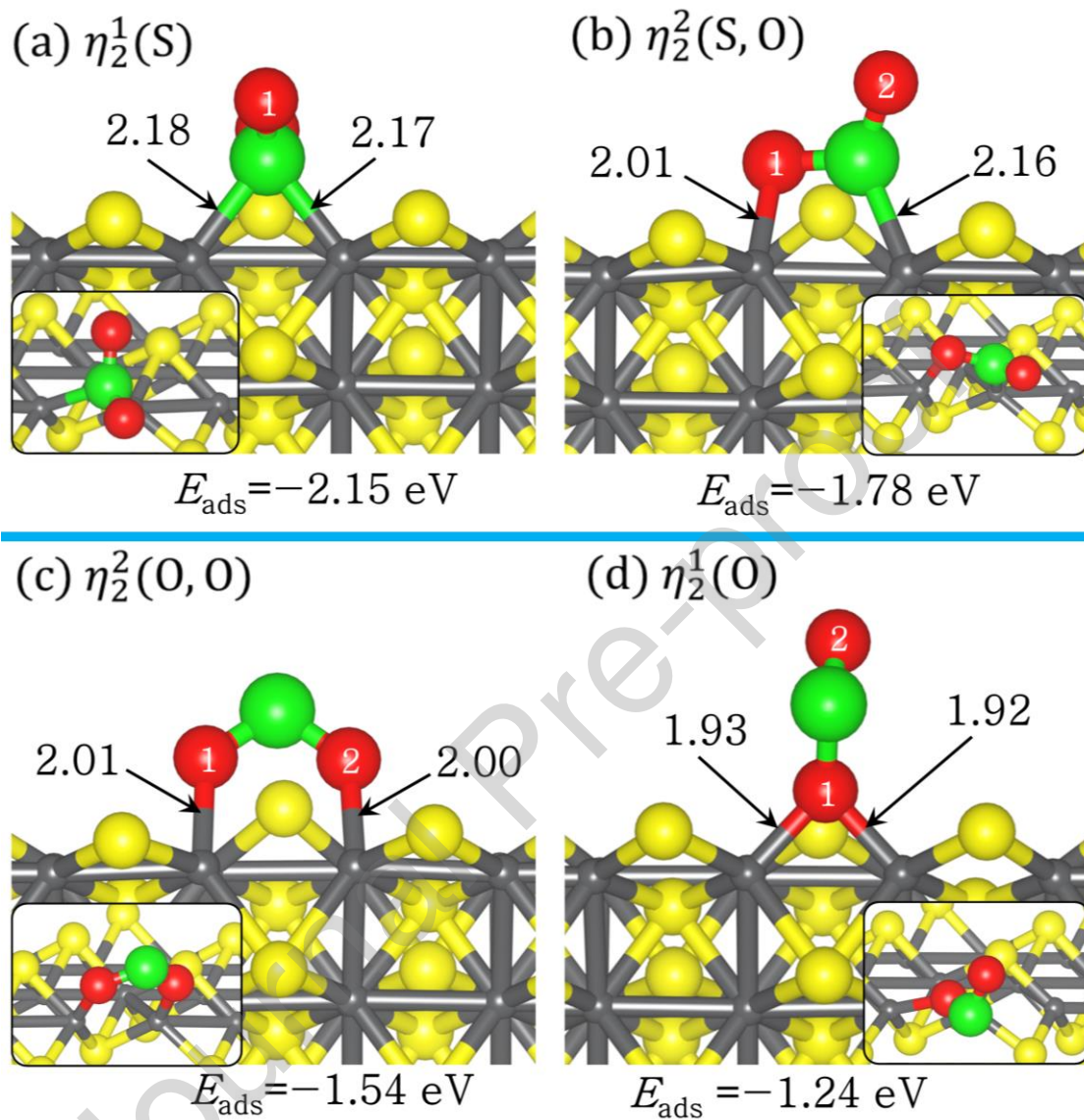


Figure 6: The electron density difference isosurface contours upon SO₂ adsorption at FeS(011) (top, a1) and at FeS(111) (down, b1) surfaces, showing regions of electron density accumulation (brown) and depletion (purple) by 0.03 e/Å³. The corresponding partial DOS projected on the interacting surface Fe *d*-states and on the S and O *p*-states of the adsorbed SO₂ molecule (a2, b2).

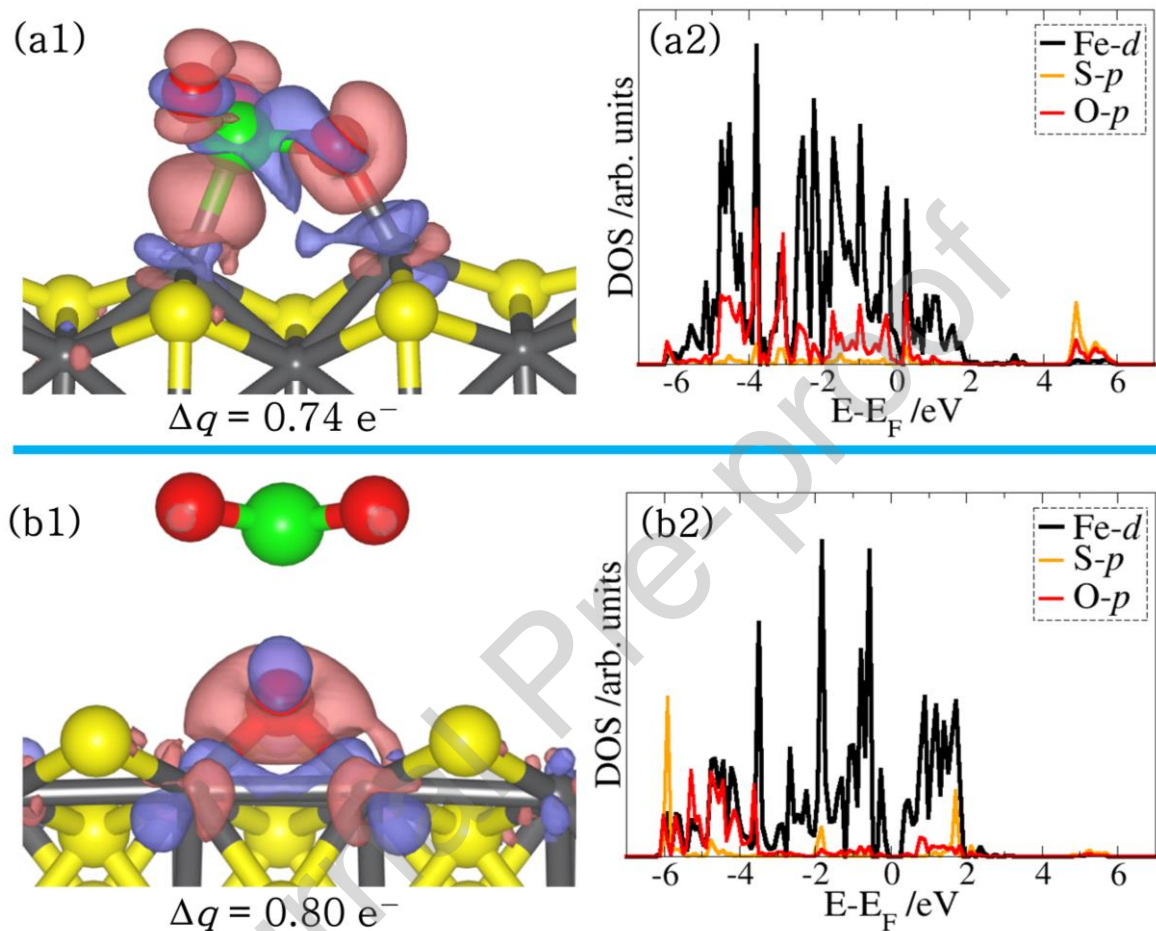


Figure 7: Optimized adsorption geometries of SO_3 on FeS (011) surface. The inserts show top views. (Colour code: Fe = grey, S_{slab} = yellow, $\text{S}_{\text{molecule}}$ = green, and O = red).

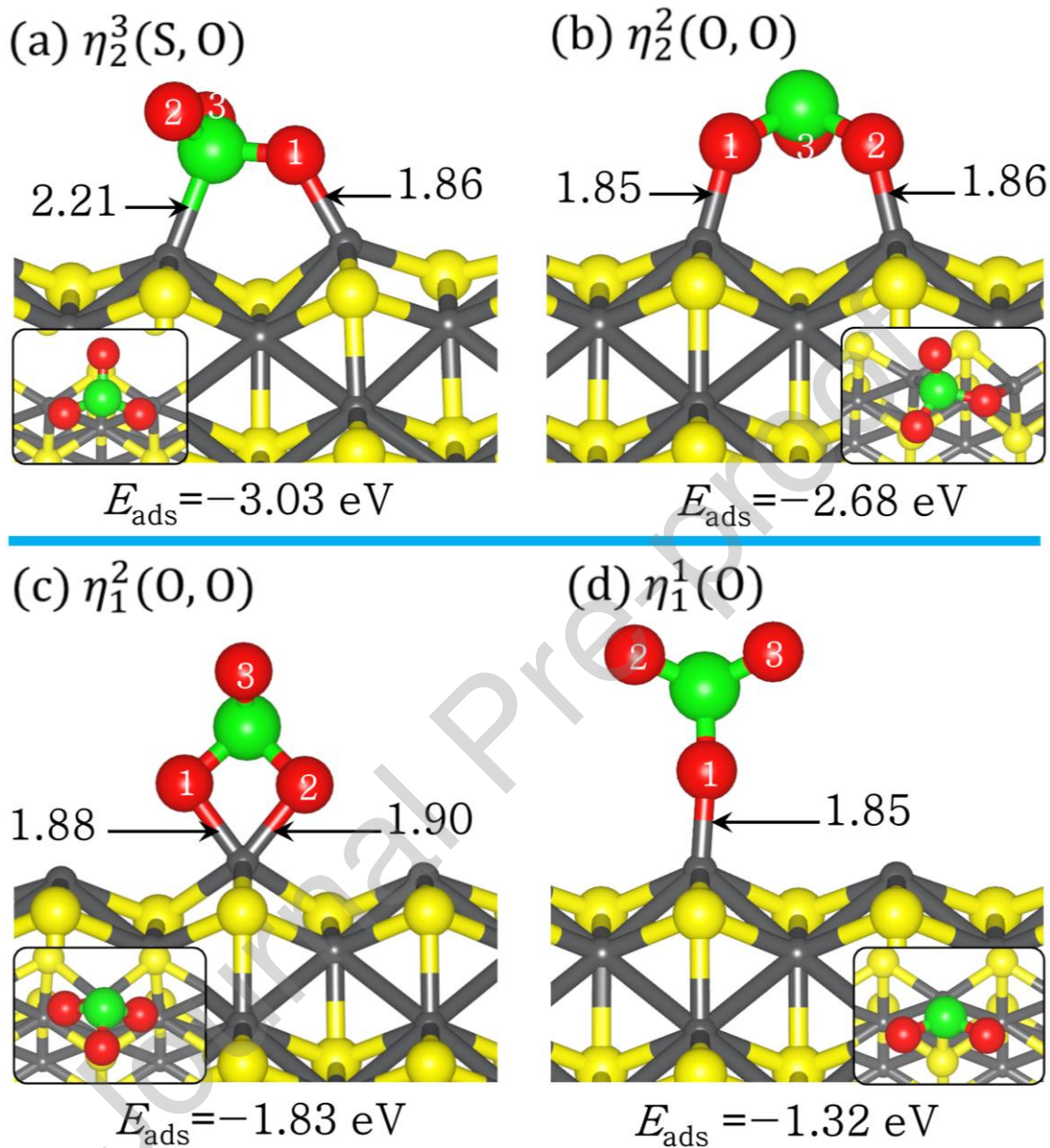


Figure 8: Optimized adsorption geometries of SO_3 on FeS (111) surface. The inserts show top views. (Colour code: Fe = grey, S_{slab} = yellow, $\text{S}_{\text{molecule}}$ = green, and O = red).

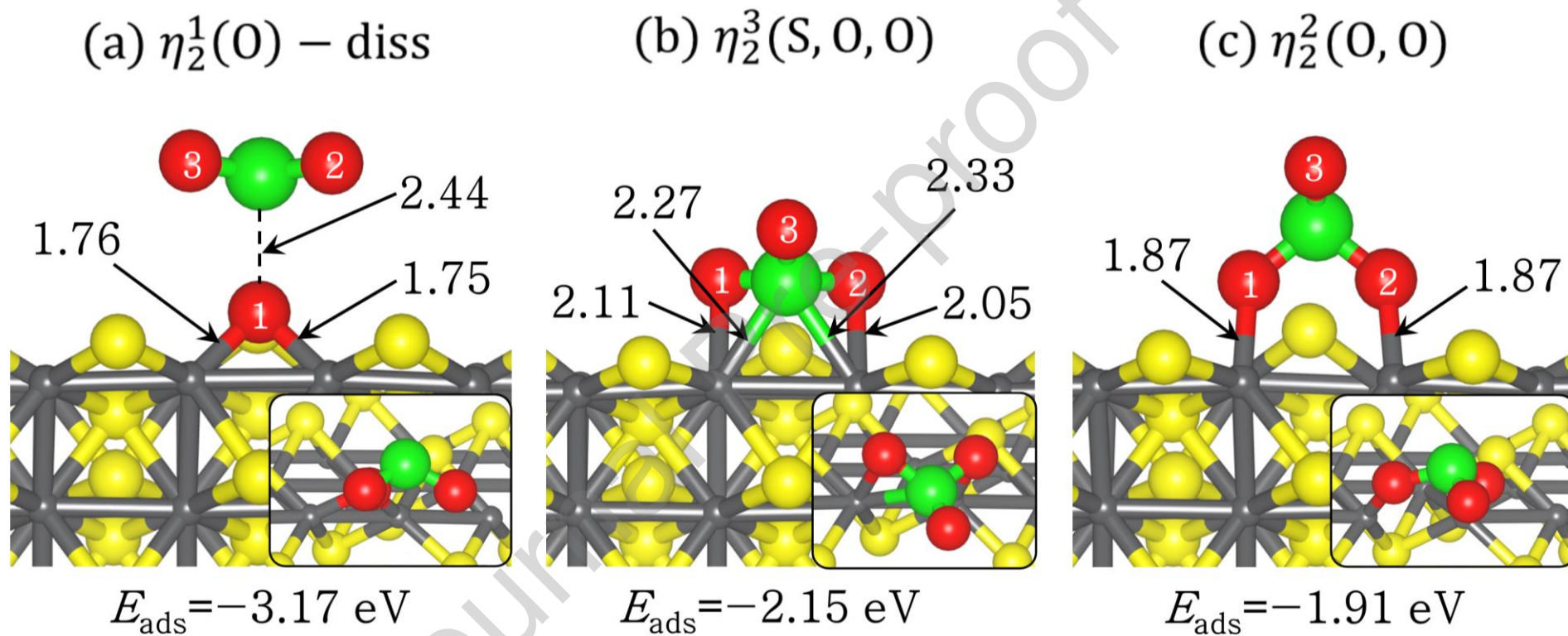


Figure 9: The electron density difference isosurface contours upon SO_3 adsorption at FeS(011) (top, a1) and at FeS(011) (down, b1) surfaces, showing regions of electron density accumulation (brown) and depletion (purple) by $0.03 \text{ e}/\text{\AA}^3$. The corresponding partial DOS projected on the interacting surface Fe d -states and on the S and O p -states of the adsorbed SO_3 molecule (a2, b2).

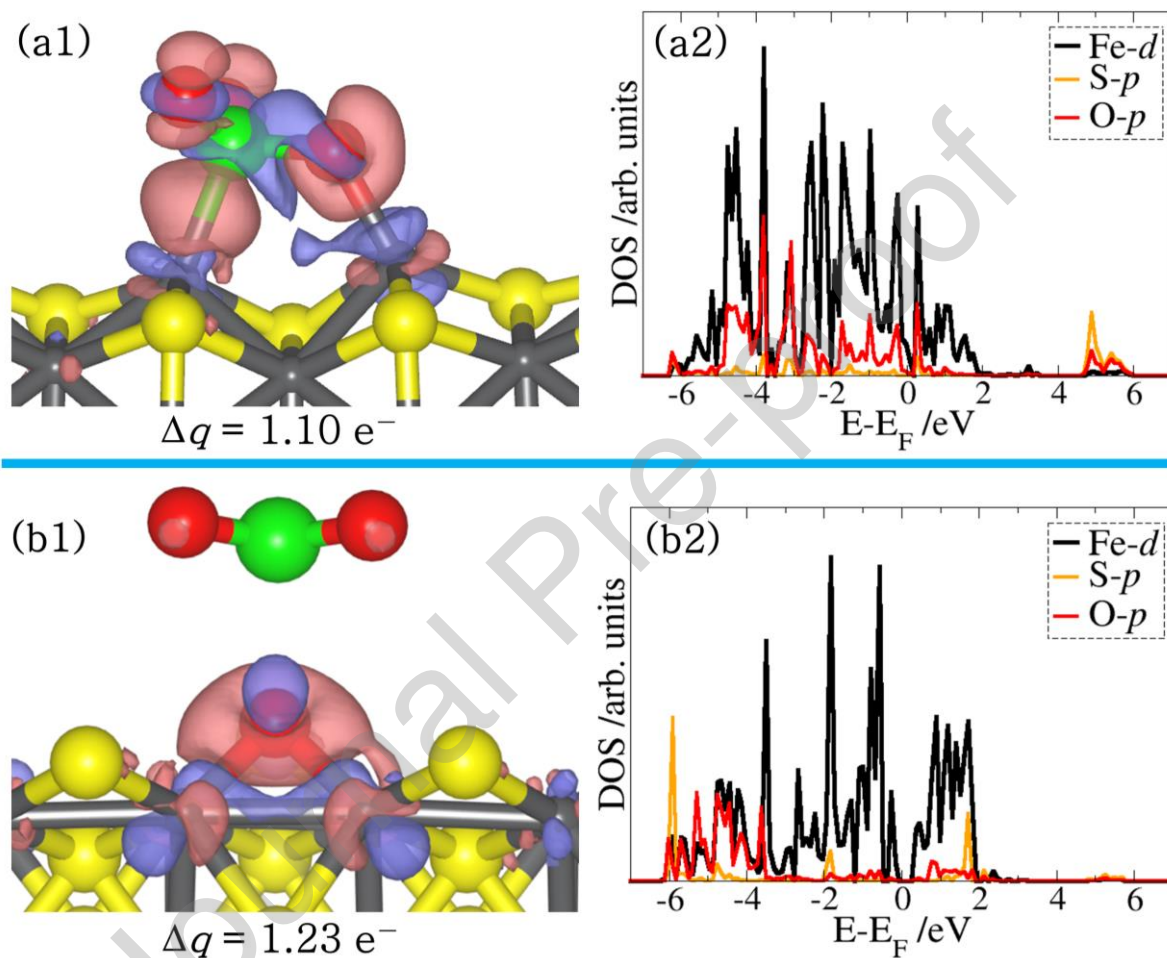


Figure 10: Optimized structures for the initial (IS), transition (TS), and final (FS) states of the most favourable path for the dissociation of SO₂ on the FeS(011) surface.

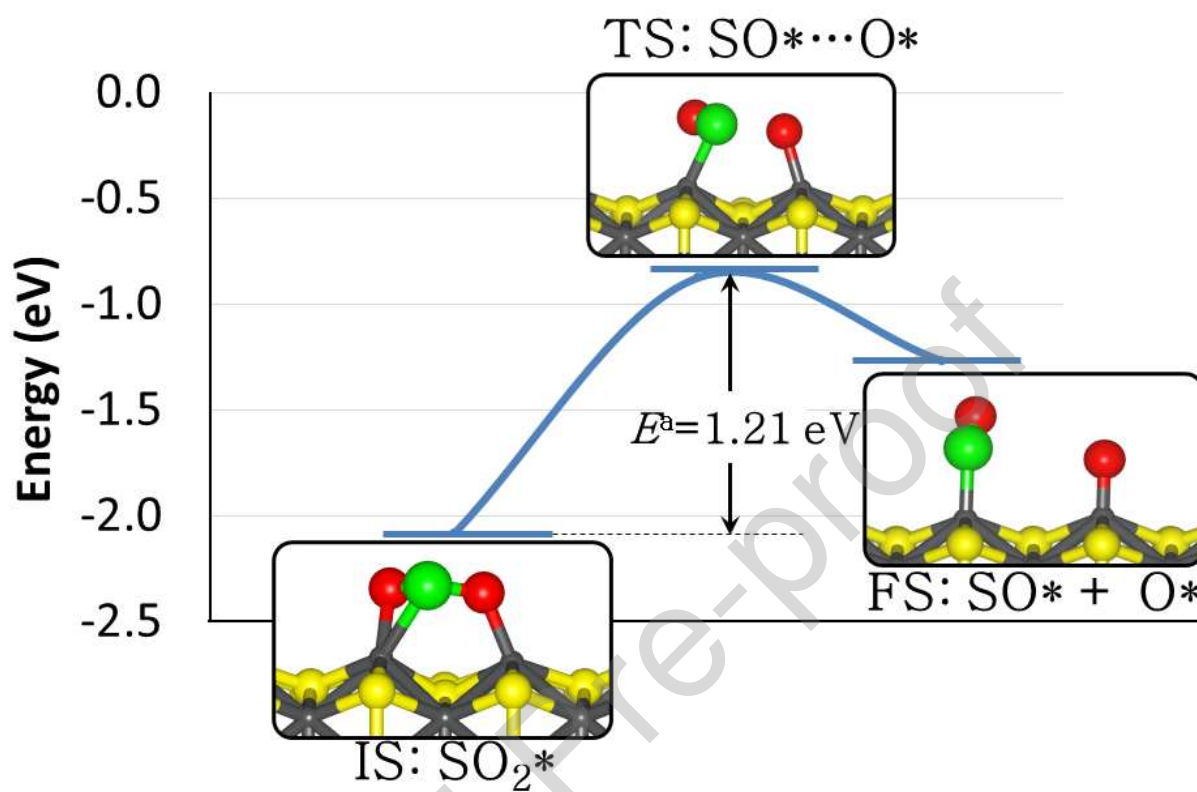


Figure 11: Optimized structures for the initial (IS), transition (TS), and final (FS) states of the most favourable path for the dissociation of SO_2 on the $\text{FeS}(111)$ surface.

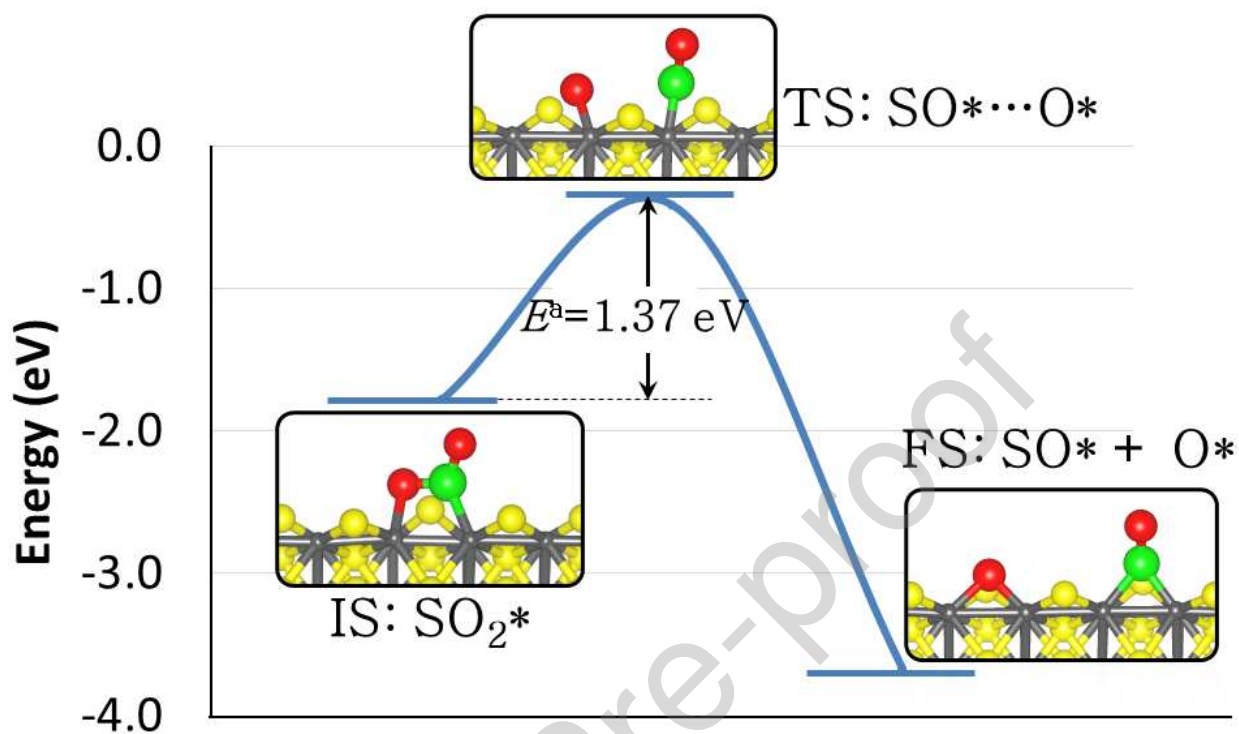
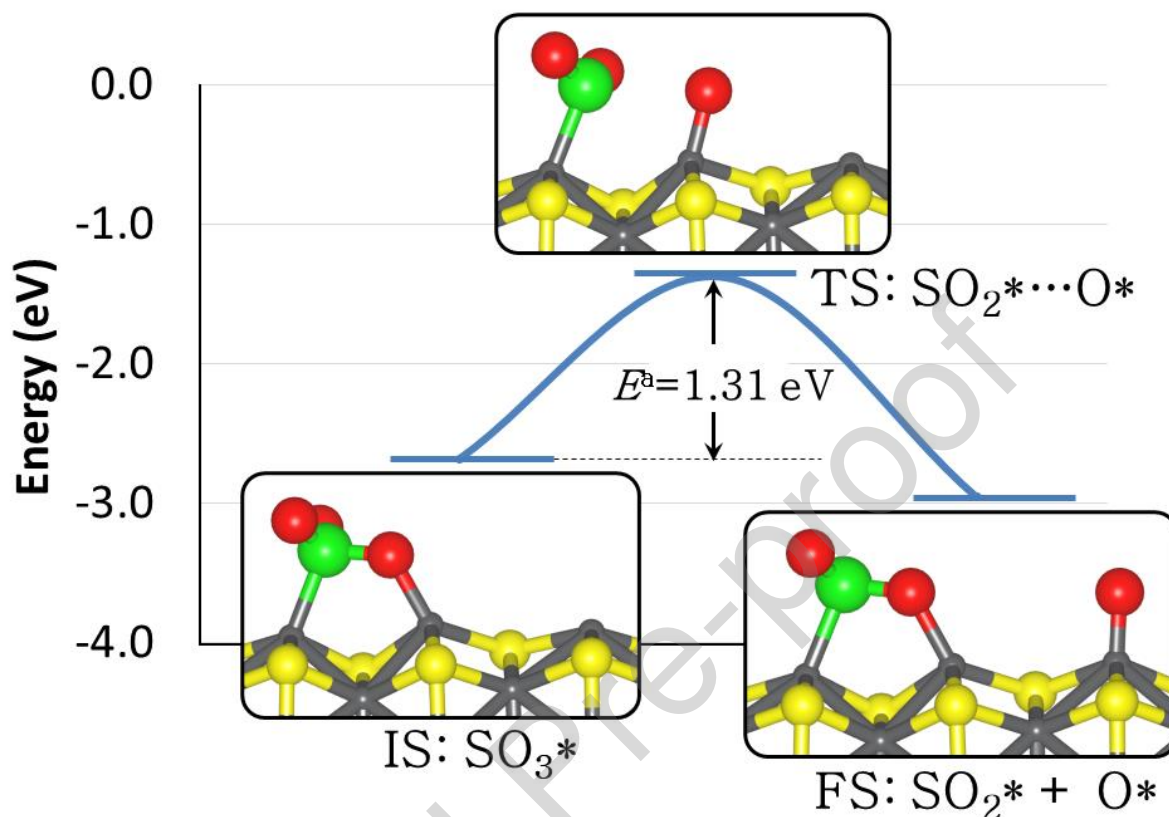


Figure 12: Optimized structures for the initial (IS), transition (TS), and final (FS) states of the most favourable path for the dissociation of SO₃ on the FeS(011) surface.



CRedit authorship contribution statement

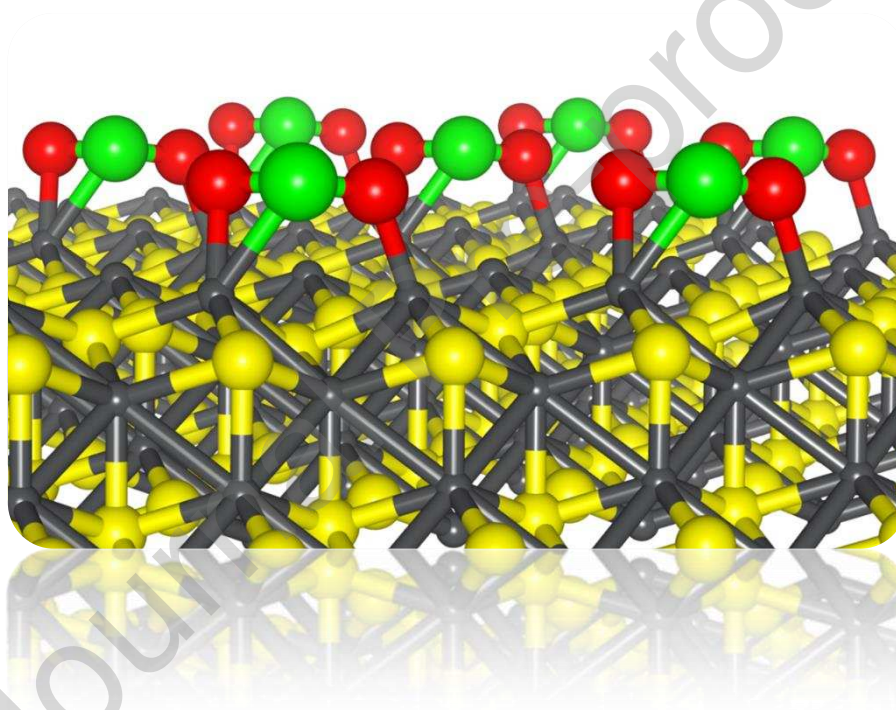
M.S.; T.T.O.; F.U.B.; T.A.; C.K.U.; A.M.T.; J.A.; G.K.K.; I.A.O. equally contributed and responsible for data curation, formal analysis, visualization, and writing of original draft. N.Y.D is responsible for funding acquisition, project conceptualization, administration, supervision, and writing - review and editing of manuscript.

Declaration of Competing Interest

☒ The authors declare that they have no known competing financial interests or personal relationships that could have appeared to influence the work reported in this paper.

☐ The authors declare the following financial interests/personal relationships which may be considered as potential competing interests:

Graphical Abstract



Highlights

- Sulfur oxides (SO₂ and SO₃) adsorption on layered FeS surfaces are characterized.

- The adsorption process is characterized by significant charge donation from the interacting surface Fe sites to the SO_x species.
- S–O bond activation and elongation is observed and confirmed via vibrational frequency analyses.
- The thermodynamics and kinetics of SO_x dissociation are analyzed.